UC Irvine
UC Irvine Previously Published Works

Title

A structural analysis of M protein in coronavirus assembly and morphology

Permalink

Journal

ISSN

Authors

Neuman, Benjamin W
Kiss, Gabriella
Kunding, Andreas H
et al.

Publication Date

DOI

Peer reviewed

A structural analysis of M protein in coronavirus assembly and morphology

Benjamin W. Neuman [a,*], Gabriella Kiss [a], Andreas H. Kunding [d,f], David Bhella [i], M. Fazil Baksh [b],
Stephen Connelly [c], Ben Droese [c], Joseph P. Klaus [l], Shinji Makino [h], Stanley G. Sawicki [j], Stuart G. Siddell [k],
Dimitrios G. Stamou [d,e,f], Ian A. Wilson [c], Peter Kuhn [c], Michael J. Buchmeier [g]

[a] School of Biological Sciences, University of Reading, RG6 6AJ, UK
[b] School of Mathematical and Physical Sciences, University of Reading, RG6 6AJ, UK
[c] The Scripps Research Institute, La Jolla, CA, USA
[d] Bio-Nanotechnology Laboratory, Department of Neuroscience and Pharmacology, University of Copenhagen, Denmark
[e] Nano-Science Center, University of Copenhagen, Denmark
[f] Lundbeck Foundation Center for Biomembranes in Nanomedicine, University of Copenhagen, Denmark
[g] The University of California, Irvine, CA, USA
[h] The University of Texas, Medical Branch, Galveston, TX, USA
[i] Medical Research Council Virology Unit, Glasgow, UK
[j] University of Toledo, OH, USA
[k] University of Bristol, BS8 1TH, UK
[l] University of Vermont, Burlington, VT, USA

ARTICLE INFO

ABSTRACT

The M protein of coronavirus plays a central role in virus assembly, turning cellular membranes into workshops where virus and host factors come together to make new virus particles. We investigated how M structure and organization is related to virus shape and size using cryo-electron microscopy, tomography and statistical analysis. We present evidence that suggests M can adopt two conformations and that membrane curvature is regulated by one M conformer. Elongated M protein is associated with rigidity, clusters of spikes and a relatively narrow range of membrane curvature. In contrast, compact M protein is associated with flexibility and low spike density. Analysis of several types of virus-like particles and virions revealed that S protein, N protein and genomic RNA each help to regulate virion size and variation, presumably through interactions with M. These findings provide insight into how M protein functions to promote virus assembly.

© 2010 Elsevier Inc. All rights reserved.

1. Introduction

Every type of virus architecture has its own structural constraints. In other words, there is a limit to the variation in shape, size or protein configuration that can be realized by a particular set of structural proteins. When this tolerance is exceeded, the result becomes uncertain: it is possible that the assembly process may fail, produce misshapen but otherwise infectious particles, or yield non-infectious particles. Pleomorphic enveloped viruses represent the most extreme cases of natural variation during assembly. Pleomorphic virions can vary considerably in size, as in the case of arenaviruses (Neuman et al., 2005) or shape, as in the case of influenza A virus (Harris et al., 2006). Although this variation has been documented, little is known about how the assembly components shape the overall particle architecture. Our understanding of virus assembly has practical implications: a

new generation of HIV-1 assembly inhibitors acts at the level of particle architecture by reducing the fidelity of the assembly process (Tang et al., 2003) or by blocking connections between Gag proteins (Sticht et al., 2005).

In this study we have chosen to analyze the relationship between composition and architecture for three pleomorphic coronaviruses: *Mouse hepatitis virus* (MHV), *Severe acute respiratory syndrome coronavirus* (SARS-CoV) and *Feline coronavirus* (FCoV). Recent electron microscopy studies have confirmed that coronavirus particles vary considerably in size, and so can safely be described as pleomorphic. However, there is disagreement over the extent of variation in virion shape (Barcena et al., 2009; Beniac et al., 2006; Neuman et al., 2006; Risco et al., 1996), although a range of morphologies is represented in each study. These three coronaviruses make an interesting dataset because each is built from a conserved set of components, but amino acid identity between the homologous structural proteins is typically less than 30%.

Four structural proteins are important for coronavirus infectivity: the integral membrane protein M adapts a region of membrane

---

for virus assembly and captures other structural proteins at the budding site, the N protein chaperones and protects the viral RNA genome, spikes consisting of three copies of the S glycoprotein promote receptor-binding and membrane fusion, and the small membrane protein E is present in sub-stoichiometric amounts and acts as an enhancer of budding (Hogue and Machamer, 2007). In this study, we will focus on the role of M in assembly and in determining particle morphology.

M proteins from MHV (Klumperman et al., 1994; Rottier and Rose, 1987), FCoV (Klumperman et al., 1994), SARS-CoV (Nal et al., 2005), *Infectious bronchitis virus* (Machamer and Rose, 1987), *Transmissible gastroenteritis virus*, (TGEV) (Klumperman et al., 1994) and *Bovine coronavirus* (Nguyen and Hogue, 1997) are targeted to the vicinity of the Golgi apparatus. Reverse genetic studies and VLP assembly studies suggest that M protein promotes assembly by interacting with viral ribonucleoprotein (RNP) and S glycoproteins at the budding site (de Haan et al., 1999; Escors et al., 2001a; Escors et al., 2001b; Kuo and Masters, 2002; Narayanan et al., 2000; Nguyen and Hogue, 1997; Opstelten et al., 1995; Sturman et al., 1980), and by forming a network of M–M interactions that is capable of excluding some host membrane proteins from the viral envelope (de Haan et al., 2000; Neuman et al., 2008b). M proteins interact through both the transmembrane domain and endodomain (de Haan et al., 2000). M can also interact with RNA that carries the genomic packaging signal (Narayanan et al., 2003). Coronavirus assembly is then completed at the membrane of a pre-Golgi compartment, as shown most recently in a tomography study of intracellular structures involved in virus replication and assembly (Knoops et al., 2008). Packets of virions are then shuttled out of the cell along the secretory pathway (reviewed in (Hogue and Machamer, 2007)). The minimum requirement for MHV virus-like particle (VLP) production is co-expression of M and E proteins (Vennema et al., 1996), although in some expression systems, the additional co-expression of N increases the efficiency of VLP production (Boscarino et al., 2008).

Recent studies have begun to reveal the structure of the coronavirus pre-fusion spike (Li et al., 2005), N protein (Chen et al., 2007; Fan et al., 2005; Huang et al., 2004; Jayaram et al., 2006; Saikatendu et al., 2007; Schutze et al., 2006), the hemagglutinin-esterase protein, which is found on some group 2 coronaviruses (Zeng et al., 2008), and the E protein (Pervushin et al., 2009). Also, transmembrane features have been identified as M on SARS-CoV, MHV, FCoV and TGEV particles using cryo-electron microscopy (Neuman et al., 2006) and cryo-electron tomography (Barcena et al., 2009), but the structure of M remains poorly characterized. The lack of detailed structural and functional information is largely due to its small size, close association with the viral envelope and a tendency to form insoluble aggregates when perturbed (Lee et al., 2005).

In this study we have attempted to provide a better understanding of the structure and function of M protein. First, we have used cryo-EM and tomography to probe the structure of M in the envelope of MHV, SARS-CoV and FCoV virions. Second, we have analyzed the structure of the MHV M protein in VLPs that lack S and RNP. This is because identification of M in electron micrographs of virions is complicated by the presence of transmembrane regions of spikes and RNP, and, more importantly, intermolecular interactions could potentially affect coronavirus morphology, including M–M, M–E, M–N, M–S, M–RNA and N–RNA interactions (reviewed in (Hogue and Machamer, 2007)), palmitin-mediated interactions involving S and E (Boscarino et al., 2008; Lopez et al., 2008; Thorp et al., 2006), and envelope stretching caused by the packaged helical ribonucleoprotein (Barcena et al., 2009). Together, these experiments reveal new facets of the structure and function of M, and demonstrate how pleomorphicity can be harnessed to reveal the function of membrane protein networks.

2. Materials and methods

2.1. Virus preparation

Growth, purification and imaging of SARS-CoV from Vero-E6 cells, FCoV from AK-D cells and MHV-OBLV60 (Gallagher et al., 1991) from DBT cells has been described previously (Neuman et al., 2006). A small plaque mutant derived from MHV-A59, called MHV-sp1, was isolated by plaque purification from the medium from persistently infected 17 clone 1 (17cl-1) cells that had survived infection with MHV-A59 and had been passaged more than 40 times (Sawicki, 1987). The MHV-sp1 S glycoprotein is not cleaved at the S1-S2 boundary and it is resistant to cleavage by trypsin, unlike the S-glycoprotein of MHV-A59. MHV-sp1 was purified by centrifugation. First, the virus from 450 ml of infected cell supernatant ($\sim 5 \times 10^{11}$ pfu) was pelleted by centrifugation for 3 h at 24,000 rpm at 4 °C using an SW28 rotor. The pellet was allowed to dissolve on ice overnight in buffered saline (0.15 M NaCl, 20 mM HEPES, pH 6.8). The 6 ml of the suspended virus was layer on top of linear gradient of 40% (w/w) potassium tartrate, 20 mM HEPES, pH 7.4 (bottom) to 15% (w/w) glycerol, 20 mM HEPES, pH 7.4 (top) and subjected to isopycnic centrifugation in a SW28 rotor (3 h at 24,000 rpm at 4 °C). The resulting milky band of virus was diluted with buffered saline and pelleted by centrifugation for 3 h at 24,000 rpm at 4 °C using an SW28 rotor. The pellet was allowed to dissolve on ice overnight in 1 ml of buffered saline.

2.2. VLP and SUV$_{100}$ preparation

VLPs were produced by transfecting HEK-293T cells with pCAGGS expression vectors encoding M, E and N from MHV-A59 (Lokugamage et al., 2008). Briefly, flasks of near-confluent cells comprising approximately 1.5 m^2 of total culture area were transfected with plasmid DNA using Lipofectamine and "Plus" reagent (Invitrogen) according to an appropriately scaled version of the manufacturer's protocol. Virus-like particles were precipitated from culture medium 48 h after transfection using 10% polyethylene glycol and 2.2% w/v NaCl, then further purified by 10–30% sucrose density gradient ultracentrifugation as described previously (Neuman et al., 2008a).

Production and cryo-EM of unilamellar phospholipid vesicles (SUV$_{100}$) created from a blend of 80 parts 1,2-dioleoyl-*sn*-glycero-3-phosphocholine, 10 parts 1,2-dioleoyl-*sn*-glycero-3-[phospho-*rac*-(1-glycerol)], 2 parts 1,2-distearoyl-*sn*-glycero-3-phosphoethanolamine-N-[biotinyl(polyethylene glycol)2000], and 1 part 3,3′-dioctadecyl-oxacarbocyanine perchlorate has been described previously (Kunding et al., 2008).

2.3. Cryo-EM and tomography

Cryo-EM was done using standard low-dose imaging conditions. Images of MHV-OBLV60, VLPs and FCoV were recorded using Leginon (Suloway et al., 2005). Cryo-electron tomography of MHV-sp1 was done using a JEOL JEM-2200FS microscope with energy filter operated at 200 kV and 25,000 times magnification. Specimens were tilted along one axis through 140°, from +70° to −70°, and images were recorded to a 4 × 4 k CCD at a nominal resolution of 5.3 Å per pixel. Tomographic reconstruction was performed using the imod software suite (Kremer et al., 1996) by fiducial alignment of 10 nm gold particles in tilted images. Two-fold binning was performed at the time of imaging to produce a model with a calibrated resolution of 10.6 Å per pixel. Details of the equipment and conditions used in conventional cryo-EM are provided in Table 1.

Table 1
Microscopy conditions and particle count.

	Microscope	Imaging	kV	Defocus (µm)	Å/pixel	Images	Particles	Vesicles
SUV$_{100}$	CM-120	1 k CCD	120	[a]	7.5	36	-	479
SARS-CoV	CM-120	Scanned film	120	2.3–5.1[b]	1.8	16	609	10
FCoV	Tecnai F20	4 k CCD	120	2.3–4.3[b]	2.3	140	466	25
EM	Tecnai F20	4 k CCD	120	1.8–2.8	2.3	46	107	85
EMN	Tecnai F20	4 k CCD	120	1.7–3.0	1.4–2.3	139	1094	15
MHV-OBLV60	Tecnai F20	4 k CCD	120	2.0–3.3	2.3	74	338	16
MHV-sp1	JEM-2200FS	4 k CCD	200	3.0	10.6	3[c]	206	0

[a] Not reported.
[b] Conventional cryo-EM images taken at a defocus of −3.3 µm or closer to focus were used for two-dimensional image analysis.
[c] Denotes complete tomograms.

2.4. Image analysis

Before analysis, image contrast was inverted so that protein density appeared white rather than black. We corrected for the effects of phase reversal in the contrast transfer function using the EMAN module ctfit (Ludtke et al., 1999). The images used for two-dimensional reconstructions displayed Thon rings, which indicate the presence of image data, to 8–16 Å resolution. Micrographs were filtered in Fourier space to truncate high-frequency image data beyond the last visible Thon ring using the EMAN module proc2d. We then selected small images showing M using the EMAN module boxer.

Image clustering and refinement of class averages was performed using the startnrclasses and classalign2 modules. Full contrast transfer function correction was implemented during construction of class averages using classalign2. The clearest, most coherent images of M densities were obtained when correction was applied through 17 Å resolution.

For radial density analysis to assess the location of S, M and the RNP inside the virion, quadrants of particles were selected to minimize the distortion caused by small variations in curvature. Quadrants were selected for inclusion in the final average based on clarity and contrast in the envelope region. For radial density analysis of M$_{COMPACT}$ and M$_{LONG}$, radial density maps were constructed by selecting and aligning numerous small wedges centered at the particle edge, which were then averaged. Radial density analysis was performed using the SPIDER image analysis suite (Frank et al., 1996), and was normalized to the brightest and darkest datapoints, which were assigned relative brightness values of 100% and 0%, respectively. The signal from the envelope region was used as a fiducial mark for normalization of image intensity and alignment of radial density profiles.

2.5. Measurement and categorization

Two observers recorded two sets each of orthogonal measurements of the longest and shortest visible diameter of each virion or VLP, so that contributions of observer bias and measurement variation could be factored into our analysis. Average diameter (d_{AVG}) was taken as a measure of particle size, and a ratio of the longest to the shortest visible diameter (d_{MAX}/d_{MIN}), was taken as a measure of particle shape (Supplementary Fig.S1). Diameters were measured to the outer edge of the membrane, leaving out spikes. Particles were excluded if part of the membrane was outside the captured image area, or if the membrane overlapped with the carbon support layer or another particle. Multilamellar, overlapping or tubular SUV$_{100}$ particles, and exosomal vesicles that appeared to have inner contents or membrane-embedded proteins were also excluded.

To assess the precision of our measurements, the distance between lipid bilayer headgroup densities was measured repeatedly by two observers. The distance between the brightest parts of the lipid bilayer on vesicles matched expected results to within 1 nm (Nagle and Tristram-Nagle, 2000). Measurements of the longest and shortest diameter of vesicles were less precise, perhaps due to combined errors in measurement and identification of the maximum and minimum particle diameter (see Supplementary Fig.S2).

In order to assess whether virus size and shape varied from one preparation to another, we compared cryo-EM images of four preparations of MHV-OBLV60 and one preparation of MHV-sp1. MHV-OBLV60 virions were fixed with 1% phosphate-buffered formalin (pH 7.0) before imaging; MHV-sp1 virions were not fixed because of differences in local biosafety regulations between EM facilities. Particle diameter was similar for all five MHV preparations (Supplementary Fig.S3). The shape of particles in two OBLV60 preparations was significantly more elongated than the other three, so these particles were excluded from shape analysis.

Before marking particles as spike-depleted or containing an envelope thickness anomaly, we revised our criteria empirically by repeatedly examining images of SARS-CoV particles and tracking the agreement between observers. The criteria were revised until inter-observer agreement was consistently greater than 80%. The final criteria for categorization were: "Does closely-packed spike decoration extend around at least half of the particle edge?" and, "Is an abnormally thin region of no less than one-twelfth the virion circumference visible in the M density layer?" Statistics describing inter-observer agreement are presented in Supplementary Fig.S2.

2.6. Cloning and expression of M$_{107–221}$

Complementary DNA was generated by reverse transcriptase PCR, and a fragment encoding amino acids 107-221 of the SARS-CoV-Tor2 M-protein was cloned into pET46Ek/LIC (Novagen, USA). The vector encodes an N-terminal poly-histidine tag and a flanking enterokinase cleavage site for tag removal. Expression of M$_{107–221}$ was achieved in BL21 (DE3) *E. coli* (Invitrogen, USA) and induced at an OD600 of 0.6–0.8 with 1 mM IPTG followed by overnight growth at 18 °C. The majority of the expressed protein was present as insoluble inclusion bodies which were subsequently refolded.

2.7. Purification and refolding

Bacteria were lysed at 4 °C using an EmulsiFlex® C-3 cell disruptor (Avestin, Canada) at 15 kpsi in lysis buffer (20 mM Tris–HCl, 100 mM sodium chloride, 10 mM dithiothreitol, 1% Triton X-100 at pH 7.0). The insoluble fraction containing the inclusion bodies was isolated by low-speed centrifugation. Pellets containing the inclusion bodies were resuspended in lysis buffer and then pelleted by centrifugation three times to remove any soluble material that was present. The pellets of insoluble material were then washed three times, as above, with wash buffer (20 mM Tris–HCl, 100 mM sodium chloride, 10 mM dithiothreitol at pH 7.0) to

remove residual detergent. The resultant white pellet was dissolved in guanidine buffer (6 M guanidine hydrochloride, 50 mM Tris–HCl, 10 mM dithiothreitol, 1 mM EDTA at pH 8.0) to a final concentration of 15 mg/ml as determined by Bradford protein assay (BioRad, USA).

Solubilized $M_{107-221}$ inclusion bodies were refolded using the rapid dilution method. Solubilized inclusion body protein was rapidly added dropwise to refolding buffer (50 mM HEPES, 200 mM sodium chloride, 1 M NDSB-201, 10 mM beta-mercaptoethanol at pH 7.0, 4 °C) to give a final protein concentration of 0.1 mg/ml. The protein was allowed to refold for 1–3 h before being applied to a 5 ml nickel affinity column (GE Healthcare, USA). The column was washed with five column volumes of binding buffer (50 mM HEPES, 200 mM sodium chloride, 10 mM beta-mercaptoethanol at pH 7.0) and refolded protein was eluted in

binding buffer supplemented with 250 mM imidazole and 1 mM EDTA. Further purification was achieved by passing 2 ml samples of the eluted protein over a pre-equilibrated Superdex™ 75 16/60 size exclusion column (20 mM HEPES, 200 mM sodium chloride, 5 mM dithiothreitol at pH 7.0). The purified monomeric protein was concentrated to 1.8 mg/ml using 0.5 ml Ultrafree Biomax 5 kDa concentrators (Millipore, USA). The protein was >95% pure as assessed by SDS–PAGE. Purified protein was stored in 20 mM HEPES, 200 mM sodium chloride, 5 mM dithiothreitol at pH 7.0.

2.8. Protein analysis

The stoichiometry of expressed M endodomain was assessed using perfluoro-octanoic acid polyacrylamide gel electrophoresis
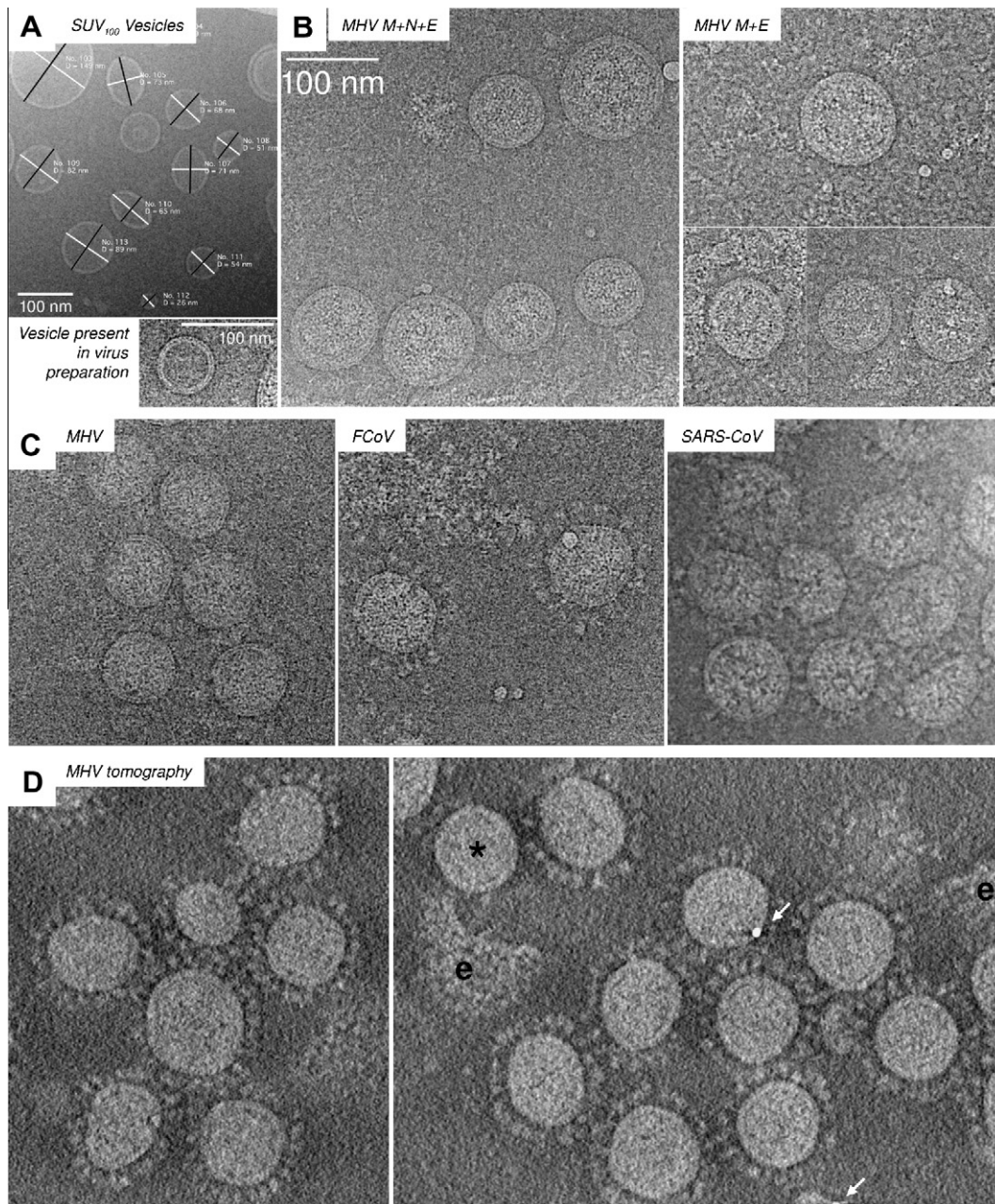

Fig. 1. Coronavirus particles and vesicles in vitreous ice. Cryo-electron micrographs of small unilamellar vesicles (A), MHV-like particles (B), three coronaviruses (C) and cryo-electron tomography of MHV (D) are shown. The longest and shortest visible diameter of each particle was measured, as shown in panel A. Viral particles were distinguished from empty exosomes by the thickness of the envelope. A spikeless particle (∗) and free viral envelopes (e) are marked. Gold particles which were used as fiducial markers in construction of the tomogram are marked with arrows.

(PFO-PAGE; (Ramjeesingh et al., 1999)). To do this, 20, 10, 5 or 2 µl of purified protein was made up to 20 µl total by adding 20 mM HEPES, 200 mM sodium chloride, 5 mM dithiothreitol, pH 7.0. Samples were incubated at either 4 or 37 °C for 1 h then separated by electrophoresis on precast 4–20% acrylamide gels in Tris–glycine buffer containing 0.5% (wt/vol) PFO. Protein was detected by SYPRO-ruby staining (Invitrogen).

3. Results

3.1. Structural analysis of coronavirus particles and VLPs

The main problem with using cryo-EM to investigate protein structure is limited resolution, which usually does not allow for the structure to be interpreted by an atomic model (Stewart and Grigorieff, 2004). As a consequence, it can be difficult to identify small features such as M in cryo-EM images.

Previous studies have used what is known about protein size, topology and function to infer the structure of spikes and RNP (Barcena et al., 2009; Beniac et al., 2006; Cavanagh, 1983; Davies and Macnaughton, 1979; Neuman et al., 2006; Risco et al., 1996). However, none of these studies produced a clear view of M, which is obscured in micrographs by the viral membrane, the C-termini of S proteins and the RNP. To better understand the structure and organization of M, we examined by cryo-EM (Fig.1A–C) and cryo-electron tomography (Fig.1D), coronavirus particles, vesicles, VLPs containing only M and E, and VLPs containing M, E and N proteins. In purified virus preparations we also found a small number of apparently protein-free empty vesicles, which presumably were released from infected cells, and which we refer to in this study as exosomes. Viruses and VLPs had thicker envelope regions than vesicles or exosomes due to the presence of M protein, as previously reported (Barcena et al., 2009; Neuman et al., 2006). The purification process used for MHV-sp1 also produced some free, spike-decorated envelopes. Free envelopes appeared thicker than ordinary phospholipid bilayers, suggesting that M was still present, but did not contain any trace of the RNP core (Fig.1D).

3.2. Extent of M inside the virion

To determine the boundaries of packaged M (Fig.2A), we examined radial density maps from groups of 18–22 empty exosomes, EM and EMN VLPs, low-spike and normal virus particles, as shown in Fig.2B. To identify individual components, we subtracted one set of appropriately scaled and aligned radial density data from another, as shown in Fig.2C.

From these data we determined that the endodomain of M extended inward ∼8 nm from the highest-density point of the outer membrane leaflet, in agreement with published measurements of MHV M protein from cryo-EM and tomography (Barcena et al., 2009; Neuman et al., 2006). The ectodomain of M did not give rise to a detectable radial density signal, suggesting that it may either be disordered or tightly membrane-associated. An area of consistent, high density which extended from 10 to 30 nm inside the particle was attributed to RNP, consistent with recent measurements by Barcena et al. (2009). Fig.2D shows that the variability in radial density was low from the virus exterior through the RNP feature, but innermost parts of the virion were highly variable. Taken together, these data show the extent of M and M-linked RNP inside the particle.

3.3. Appearance of packaged M protein

Viral particles were examined closely to identify individual M protein shapes. On most particles, M at the virion edge resembled
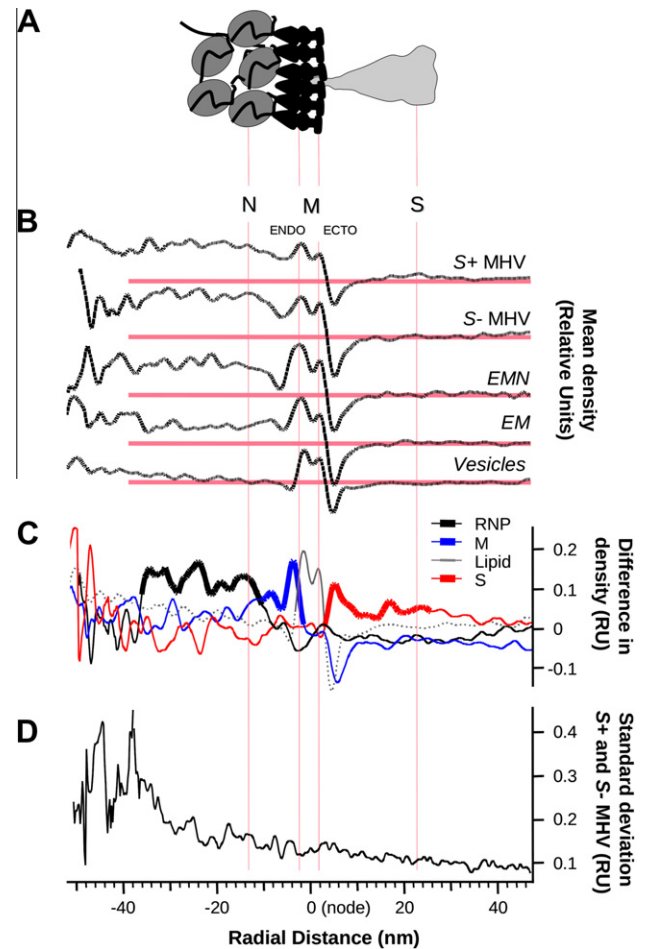

Fig. 2. Identification of M and ribonucleoprotein in viral particles. (A) A model viral envelope explains features of an MHV particle by comparing the (B) averages of ∼20 radial density distributions from MHV virus-like particles, apparently spike-depleted virions, normal virions and empty exosomal vesicles. (C) Individual features are mapped onto the radial density pattern of empty vesicles as follows: M protein (blue) is revealed as the difference between EM VLPs and vesicles, S (red) is the difference between normal and spikeless virions and ribonucleoprotein is the difference between EM VLPs and spikeless virions. (D) Differences in the consistency of core and envelope organization are revealed from the standard deviation of 40 MHV radial density plots.

tightly packed lines crossing the membrane and contacting the RNP (Fig.3). Small M-free areas which may represent budding scars were occasionally visible at the edge of virions and VLPs (Fig.3A). The observation that M remained tightly packed even on particles with excess M-free membrane provides structural validation of the existence of M–M interactions. The observation that M densities appear to make contact with the RNP core likewise can be taken as evidence of M–N or M–RNA interactions.

On a few particles, some of the M-like protein had a compact, blurred appearance and did not appear to make contact with the RNP. We have called the common form M_{LONG} and the short, blurred form $M_{COMPACT}$. Viral spikes can be seen on both M_{LONG} and $M_{COMPACT}$, but not on M-free membranes (Fig.3B–D). This was taken as further evidence of M–S interactions and confirmation that $M_{COMPACT}$ is likely a form of M, perhaps an alternate conformer. Enlarged images showing the features we have termed M_{LONG}, $M_{COMPACT}$ and M-free membrane are shown in Fig.3E–G. Radial density maps showing the difference in appearance between M_{LONG} and $M_{COMPACT}$ are presented in Fig.3H.

In order to express M conformation numerically, we performed radial density analysis of small sections at the particle edge where
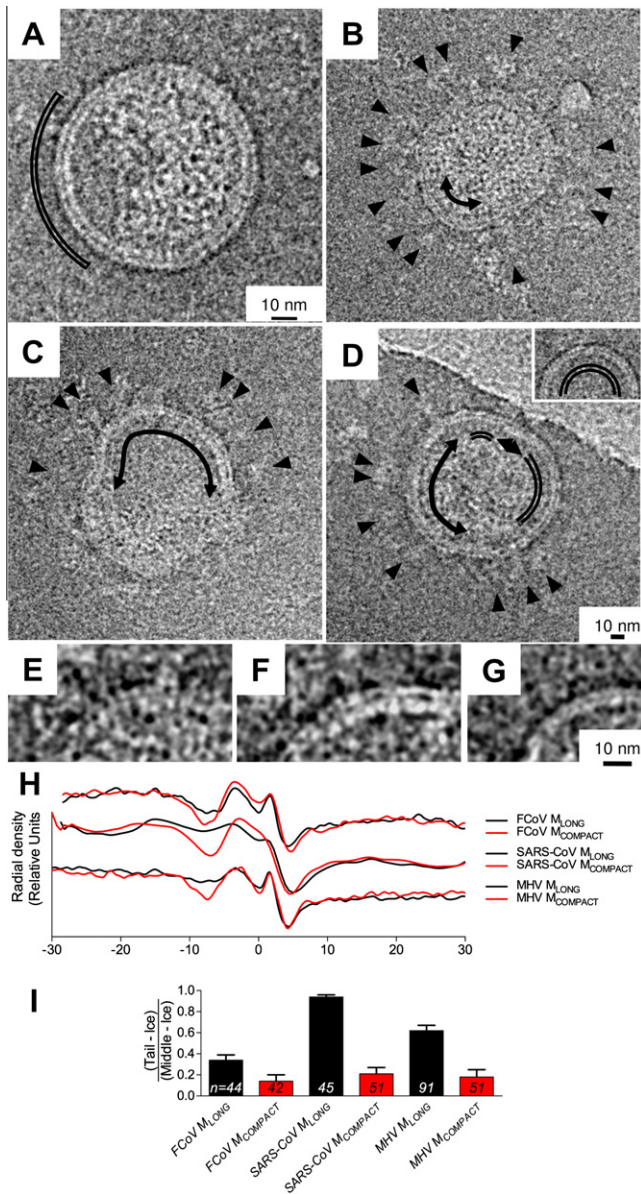
Fig. 3. Evidence for two forms of M protein in virions. Distinct rod-like M_{LONG} features can be seen in at the edge of cryo-EM images of MHV *EMN* VLPs (A) and feline coronavirus (B–F). Regions where M appears indistinct, compact and does not appear to contact the ribonucleoprotein at the particle edge are marked with curved arrows. Regions of membrane that resemble protein-free lipid bilayers (D, inset and G) are marked with a double-line. Enlargements of M_{LONG} (E), $M_{COMPACT}$ (F) and a vesicle (G) are shown below. Radial density maps (H) and M tail to body ratios (I) are shown to illustrate the difference in appearance between M_{LONG} and $M_{COMPACT}$ from three coronaviruses.

M_{LONG} or $M_{COMPACT}$ was visible. The M endodomain density consisted of the tail region, extending 6 to 8 nm into the particle where the differences between M conformations were most apparent, and the denser body region, extending 3.5 to 5.5 nm into the particle. After subtracting the density of the ice outside the particle to correct for differences in background and scaling image brightness to a common mean, the ratio of M tail to middle was calculated for each virion or VLP. We found that the density in the "tail" region of $M_{COMPACT}$ was similar to the density of the background ice, and the peak M endodomain was higher than for M_{LONG}. To express M conformation more simply, we subtracted the background from the tail and body densities and calculated tail to body ratios for M_{LONG} and $M_{COMPACT}$ (Fig.3I). We found that the difference in tail

to body ratios was statistically significant (*T*-test, $P = 0.014$ for FCoV, $P = 2.0 \times 10^{-17}$ for SARS-CoV and $P = 3.0 \times 10^{-6}$ for MHV). This suggests that the two forms of M represent different conformations of the same peptide chain, and the distribution of density at the virion edge can be used as an approximate readout for M conformation.

We next examined M proteins in more detail by classifying, aligning and averaging similar-looking regions from particle edges to produce class averages. M_{LONG} resembles a dagger, with the ectodomain "pommel" resting on the outer membrane leaflet and the tip of the endodomain "blade" extending ~8 nm and contacting the RNP (Fig.4A-B). The endodomains of adjacent M_{LONG} particles appeared to contact each other, suggesting that M_{LONG}–M_{LONG} interactions are mediated by the endodomain of M. M_{LONG} on *EM* VLPs appeared similar to M on virions, thus confirming that M_{LONG} is formed by M in the absence of the other high-copy virion proteins S and N (Fig.4B). Some class averages of M_{LONG} also showed a distinct tilt relative to the membrane. The endodomain of M_{LONG} was resolved into two globular components with crisp borders between adjacent molecules, while the endodomain of $M_{COMPACT}$ appeared as an indistinct ellipsoid and extended only ~6 nm (Fig.4A). The two globular components of the endodomain were not distinctly observed in class averages from EM VLPs (Fig.4B), suggesting that either the conformation is only formed in the presence of N or that N forms part of the two-lobed M_{LONG}. M_{LONG} and $M_{COMPACT}$ were also visible in virtual slices through tomographic reconstructions of MHV. The difference in apparent length was most evident on tomographic slices through free envelopes, which showed thick convex M_{LONG} membranes near the center giving way to thinner variably curved $M_{COMPACT}$ membranes near the edges (Fig.5A and B).

M_{LONG} was spaced 4 to 5 nm apart in unprocessed cryo-EM images and edge view class averages (Fig.6). In axial views of M taken from the centers of *EM* and *EMN* VLPs, M sometimes appeared to form small ordered regions (Fig.6A) which could be classified, aligned and averaged to produce class averages (Fig.6B). M spacing in axial views was generally consistent with spacing in edge views (Fig.6C). While axial class averages suggest that M packing generally approximates a rhombus with sides of 4.0 and 4.5 nm and an interior angle of about 75°, the amount of heterogeneity in the unprocessed images is more consistent with a loosely-ordered network of M, as opposed to a rigid two-dimensional protein lattice.
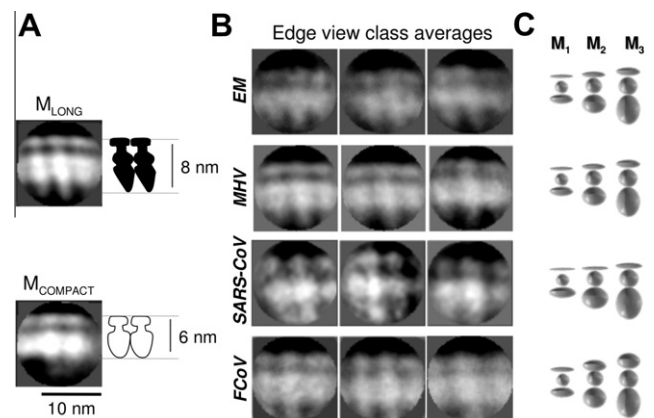

Fig. 4. Edge views of packaged M. Reference-free class averages were made from groups of 300–2000 images clipped from viral particle edges. Full contrast transfer function correction through 17 Å resolution was implemented during class average reconstruction. Edge view class averages show M_{LONG} (A, top) and $M_{COMPACT}$ (A, bottom) from MHV *EMN* VLPs. Examples of class averages showing M_{LONG} from *EM* VLPs and virions are shown in panel B. Panel C shows two-dimensional projections of M ectodomain, transmembrane domain and endodomain as ellipsoids with the width of M_{LONG} from class averages and the expected volume of one, two or three copies of M protein (right).
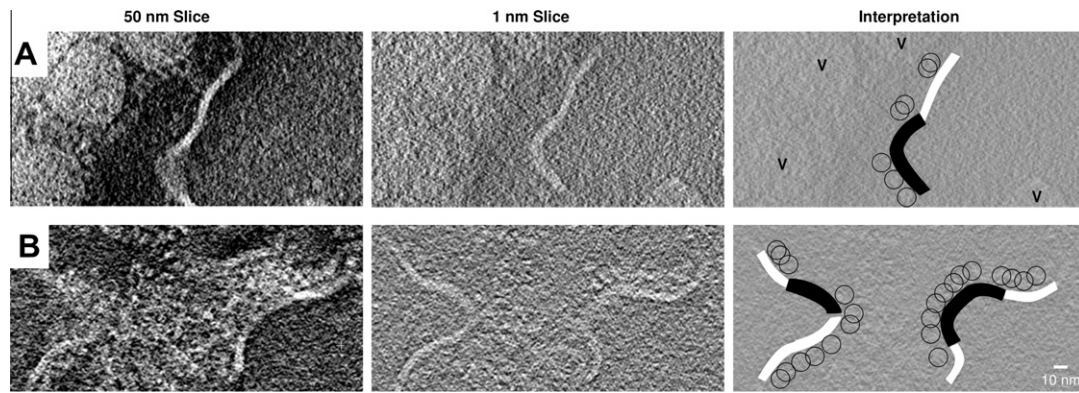
Fig. 5. Association of M$_{LONG}$ with convex, spike-decorated membranes. Panels A and B depict free viral envelopes that were found in MHV tomograms. Projections through thick (50 nm) and thin (1 nm) subtomograms are shown for comparison. Thicker regions of the membrane ascribed to M$_{LONG}$ are marked black, and thinner regions ascribed to M$_{COMPACT}$ are marked white. Visible spikes are marked with circles to demonstrate membrane topology and intact virions (V) are also indicated.
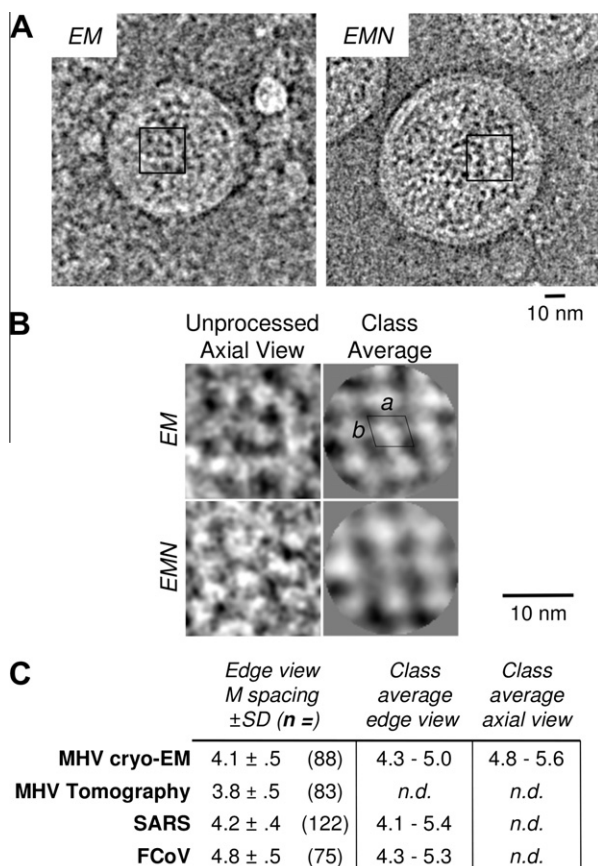

Fig. 6. Organization of M. Small areas which appear to show axial views of small clusters of organized M proteins are marked in images of VLPs (A), and enlarged below (B, left). Reference-free class averages were made from groups of 1500 (*EM*) or 3000 (*EMN*) images clipped from VLP centers. Full contrast transfer function correction through 17 Å resolution was implemented during class average reconstruction. Unit cell dimensions are approximately 4 nm (a) by 4.5 nm (b), with an interior angle of 75°. (C) Average spacing of M dimers as measured by various methods.

3.4. Oligomerization of M

Edge view class averages of M$_{LONG}$ from MHV, FCoV and SARS-CoV virions appeared about twice as large as expected for a single copy of the M protein, based on the partial specific volume of folded protein (Harpaz et al., 1994). This can be seen by comparing class averages showing M (Fig.4B) with projections of ellipsoids

with the same spacing as M, and the volume of one, two or three copies of M, (Fig.4C). This suggested that each M$_{LONG}$ and M$_{COMPACT}$ is large enough to contain at least two copies of M protein.

We next attempted to investigate the stoichiometry of purified M protein biochemically. Attempts to express SARS-CoV M protein in *E. coli* and baculovirus expression systems produced only insoluble aggregates. The largest M construct which we were able to express and purify consisted of residues 107 to 221 from SARS-CoV M, which covers the area of the endodomain from just after the third predicted transmembrane region to the C-terminus. M$_{107–221}$ was expressed as an aggregate initially, but became soluble upon refolding.

Since a fusion protein incorporating the endodomain of MHV M was shown to co-immunoprecipitate with full-length M protein (de Haan et al., 2000), and class averages suggested that adjacent M$_{LONG}$ dimers make contact via two parts of the endodomain, we decided to investigate the oligomerization of M$_{107–221}$ as a surrogate for full-length M. Soluble endodomain incubated in saline at 37 °C was present as monomers and aggregates as well as units of two, four and six, while endodomain incubated at 4 °C remained mostly monomeric (Supplementary Fig.S4). These observations support the interpretation that M functions as a homodimer.

3.5. Determinants of particle shape

In solution, the shape of a vesicle is determined by the interplay of opposing forces (Zhong-can and Helfrich, 1987). The ground state for vesicles in solution is spherical. Forces imparted by fluid motion or sample freezing in preparation for cryo-EM can temporarily distort vesicle shape. However, as a particle becomes less spherical the effects of hoop stress will increase, leading either to structural failure of the vesicle wall or driving the vesicle back to a more toward spherical, lower-stress shape.

Since enveloped virus particles and are essentially protein-decorated vesicles, we reasoned that their shape should be similar to the shape of vesicles unless modified by the effects of viral protein interactions. To test whether viral proteins significantly affected the shape of viral particles, we compared the shape of virions, VLPs and small unilamellar vesicles of the same size (SUV$_{100}$) in cryo-EM images.

In our images, vesicles ranged from round to ellipsoidal, with the average particle having a long axis 1.08 times the length of the shortest axis (Supplementary Fig.S1). The shape of MHV and *EM* VLPs did not differ significantly from the shape of vesicles. However, *EMN* VLPs were significantly rounder than the combined population of SUV$_{100}$ and endosomal vesicles (ANOVA, $P = 0.005$). Although EM particles were rounder on average than EMN

particles or vesicles, the difference was not significant due to the small sample size and heterogeneity of the EM particles. This indicates that the protein component of *EMN* VLPs provides significant resistance to the deformative forces that affected vesicles under cryo-EM conditions.

We next sought an explanation for how E, M and N proteins can make spherical vesicles more rigid. N proteins can dimerize (Chen et al., 2007) and pack helically in the presence (Barcena et al., 2009) and absence (Saikatendu et al., 2007) of RNA, but neither of these interactions alone would be expected to produce a spherical arrangement. E protein is small and not abundant enough in viral particles to be a convincing explanation for overall shape. In contrast, M is abundant, interacts with other M proteins and with membranes, which are approximately spherical. We therefore hypothesized that particle shape is controlled primarily through M.

A striking difference between M_{LONG} and $M_{COMPACT}$ is that M_{LONG} appears to contact the RNP while $M_{COMPACT}$ does not. In cryo-EM images, the internal RNP appeared to be pulled away from the particle edge where either $M_{COMPACT}$ or M-free membrane is present, as seen in Fig.3. Thus, $M_{COMPACT}$ and M-free membranes can both be viewed as local disruptions of the M–RNP interaction. To test the hypothesis that M-mediated interactions control particle shape, we compared the shape of particles in which M_{LONG} appeared to form a complete ring at the particle edge to the shape of particles in which the ring of M_{LONG} was interrupted by either a M-free membrane or $M_{COMPACT}$.

Interruption of M_{LONG} at the particle edge was associated with significant particle elongation in SARS-CoV (ANOVA, $P = 5 \times 10^{-12}$), FCoV ($P = 0.01$) and *EM* ($P = 0.03$) particles. A similar but non-significant trend was observed for MHV (Fig.7A). While a relative increase in M anomalies was correlated with particle elongation, we noted that: The relative abundance of particles with interrupted M was quite different in the three coronaviruses, while

the frequency of M anomalies was similar in MHV, EM and EMN particles. This result shows that an uninterrupted layer of M_{LONG} is a marker for spherical morphology, but suggests that there may be inherent differences in the interaction affinities and membrane-bending properties of different coronavirus M proteins.

If only M_{LONG} is associated with coronavirus-like membrane curvature, it is implicit that the ratio of M_{LONG} to $M_{COMPACT}$ should be related to local membrane curvature. To test this, we selected four parts of each particle edge, which were centered on either side of the longest and shortest particle diameter as shown in Fig.7B. Two independent observers counted the number of M dimers present and marked them as M_{LONG} or $M_{COMPACT}$. The ratio of M_{LONG} to $M_{COMPACT}$ was about the same at all of the virion ends, but the proportion of M marked as M_{LONG} on the flatter sides decreased as particles became more elongated (Fig.7C). From these results we conclude that clusters of M_{LONG} mark round membranes.

We noted that some samples of purified MHV appeared quite ellipsoidal while others were mostly round, while virion size was similar in all of the MHV preparations (Supplementary Fig.S3). Purification over sucrose density gradients would at least temporarily expose viral particles to osmotic stress. Likewise, centrifugation would necessarily expose virus particles some mechanical stress. We suspected that in some cases the purification process might change virion shape.

3.6. Conversion between M_{LONG} and $M_{COMPACT}$

To investigate whether virion shape could be changed experimentally after purification, one sample of purified virus was resuspended in HEPES-buffered 0.9% saline buffer, pH 7. Half the sample was kept in the resuspension buffer, while the other half was acidified to pH 5 for 5 min in order to simulate pH changes that might occur during entry via the endosomal route, and then re-buffered to pH 7. The shape and size of native MHV (Prep 1 in Supplementary Fig.S3) and acid-pulsed MHV (Prep 3) were examined by cryo-EM. Overall particle shape did not change significantly as a result of acidification (ANOVA, $P = 0.93$). However, the relative proportion of particles which appeared to have at least one flattened edge increased significantly after acid-treatment (Fisher's exact test, $P = 0.0001$; Fig.8A–C). In some flat-edged particles, the interior RNP appeared to have a crisp edge, which was more distant from the membrane than RNP in native particles and M had the blurred appearance characteristic of $M_{COMPACT}$ (Fig.8B). Radial density plots and M tail to body ratios demonstrate that the altered M which was more frequently found at flat edges of acid-treated particles strongly resembled $M_{COMPACT}$ from native MHV particles (Fig.8D and E). From this we concluded that transient acidification can partly convert M_{LONG} to $M_{COMPACT}$, but other factors that occur during purification can have a more dramatic effect on particle shape.

We next investigated how the expression of N affected M conformation. We compared M tail to body ratios for whole MHV VLPs to regions of MHV M_{LONG} and $M_{COMPACT}$ and found that M in EMN VLPs was nearly identical to M_{LONG} from native MHV (T-test, $P = 0.94$), while M from EM VLPs was intermediate between M_{LONG} and $M_{COMPACT}$ (Fig.8E). This suggests that intracellular N plays an important role in the formation or packaging of M_{LONG}.

3.7. Relationship between spikes and morphology

Previous studies have shown that spikes are dispensable for assembly but essential for infectivity. It was therefore surprising to find that spikeless *EM* and *EMN* VLPs were significantly larger than virions (Supplementary Fig.S1) and rare viral particles on which no spikes were visible were significantly larger than spike-decorated virions (Fig.9A), suggesting that spike incorporation
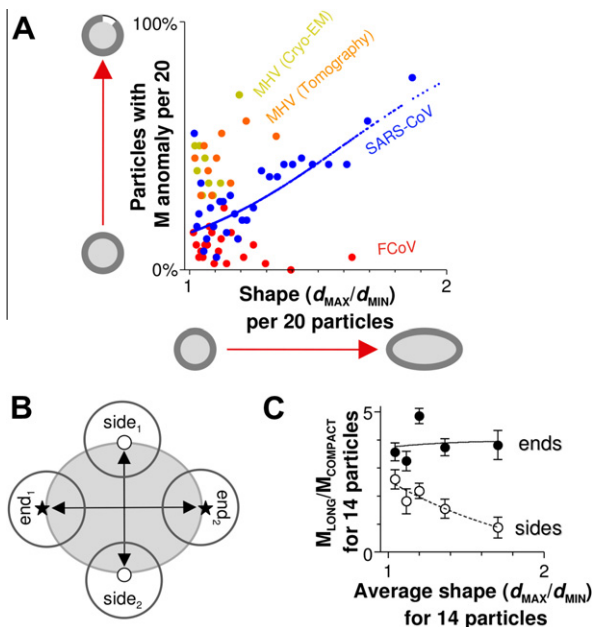

Fig. 7. Relationship between M conformation and particle shape. (A) The ratio of the longest to the shortest diameter of coronavirus particles from MHV, SARS-CoV and FCoV micrographs and MHV tomograms is plotted against the percentage of particles which had at least one anomalously thin region of membrane. Each datapoint presents the average for 20 particles of similar shape. (B) Boxes were centered on the membrane at each end (stars) and side (circles) of seventy SARS-CoV particles to examine the relationship between M-form and membrane curvature. (C) The ratio of M_{LONG} to $M_{COMPACT}$ is plotted against average particle shape. Each datapoint represents two sides or ends from fourteen particles of similar shape. (A, C) Curves were fitted by logistic regression.
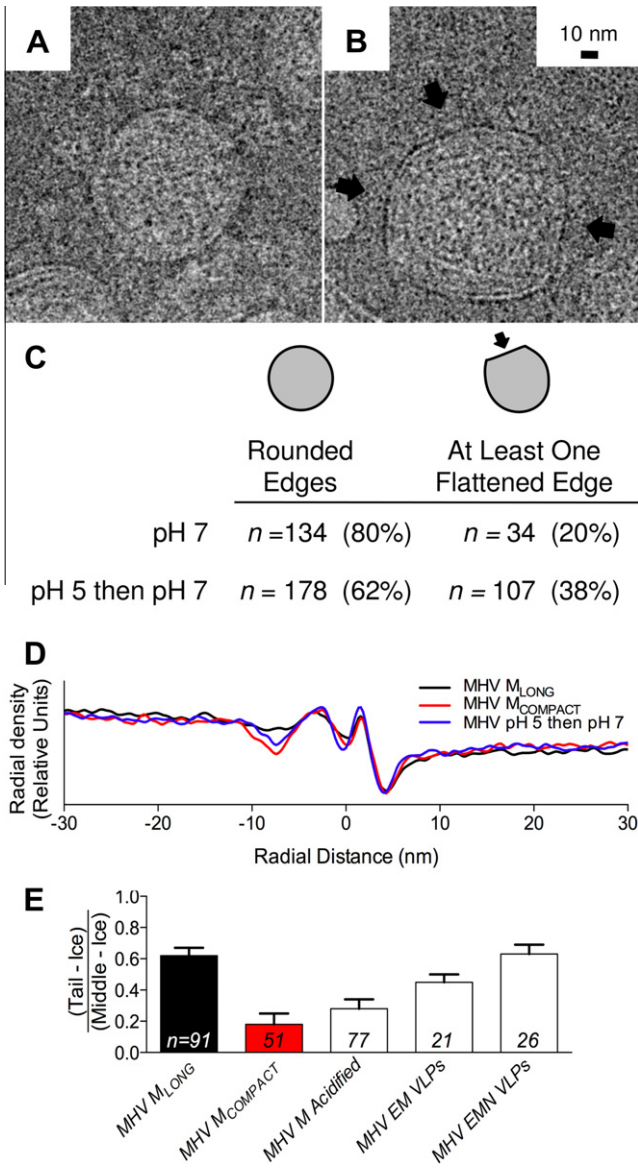
Fig. 8. Conversion between M_{LONG} and $M_{COMPACT}$. Purified MHV was imaged by cryo-EM after incubation at pH 7 (A), or a 5 min pulse at pH 5 followed by re-neutralization to pH 7 (B). Arrows in panel B point to flattened edges of the particle with the appearance of $M_{COMPACT}$. The proportion of flat-sided virions before and after acidification is shown in table form (C). Radial density maps (D) and M tail to body ratios (E) of the altered regions from acidified MHV, native EM VLPs and native EMN VLPs are shown alongside MHV M_{LONG} and $M_{COMPACT}$ data from Fig. 3h-i.

Fig. 9. Relationship of S protein to morphology. (A) The ratio of the longest to the shortest diameter of coronavirus particles from micrographs is plotted against the percentage of particles which had fewer than half the expected number of spikes visible at the particle edge. Each datapoint depicts the average and standard deviation for a group of 20 similar-sized particles. Curves were fitted by logistic regression to datasets in which the association between spike decoration and size was statistically significant (ANOVA, $P = 6.71 \times 10^{-8}$ for FCoV and 0.046 for MHV). (B) SARS-CoV particles were classified according to shape and spike distribution. The three shape categories refer to particles with d_{MAX}/d_{MIN} less than 1.1 (round), 1.1–1.4 (slightly oval) or greater than 1.4 (elongated). The number of particles of each type that were classified is listed.

was linked to envelope size. Since the size of the virus envelope is fixed at the scission stage of the budding process, we inferred that spike incorporation is linked to factors which produce small virions.

To determine which factors were linked to particle size, we measured MHV VLPs in cryo-EM images and MHV virions in tomograms, where spike decoration could be assessed in three dimensions. MHV *EM* VLPs (93 nm average diameter) were larger than *EMN* VLPs (91 nm) and spikeless MHV in tomograms (91 nm) and spike-decorated MHV (88 nm). Viral particle size decreased as particles approached the full complement of proteins and RNP (Supplementary Fig.S1), suggesting that small virions are produced as a result of the interplay between all viral components during assembly.

A few SARS-CoV particles appeared to have clusters of spikes at one or two spots on the viral envelope. Spike clusters were signif-
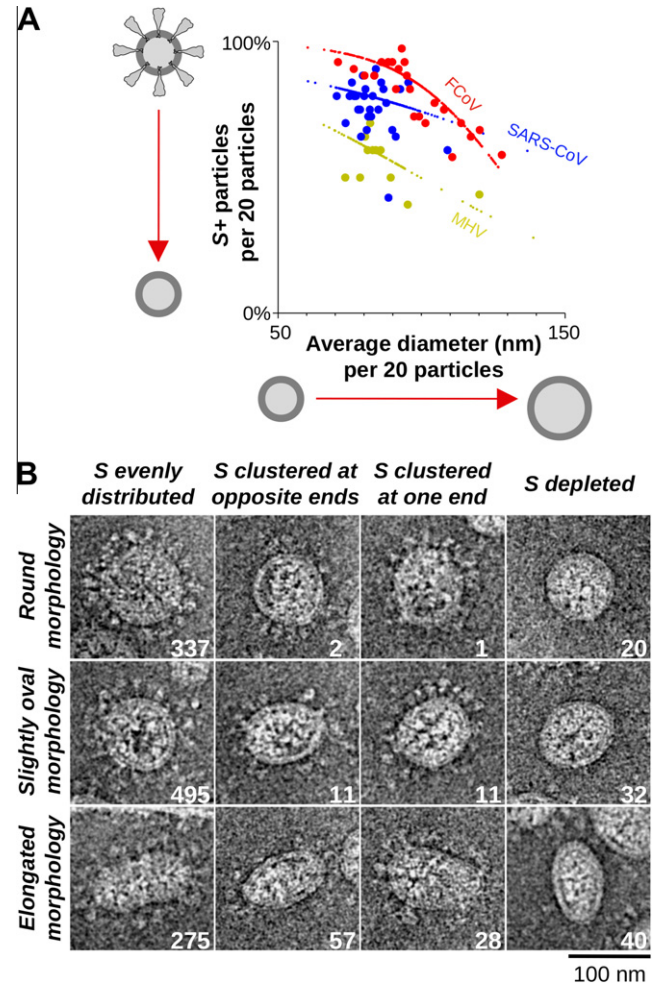
icantly associated with the curved ends of ellipsoidal particles (Fig.9B), which we had previously found to be marked by M_{LONG}. We therefore concluded that M_{LONG} is a marker of spike decoration.

4. Discussion

Here we demonstrate that a network of M has intrinsic membrane-bending properties, as recently demonstrated for the HIV-1 Gag polyprotein (Carlson et al., 2008). We report that M is functionally dimeric in viral particles, and the membrane-altering properties of M depend on interactions with other viral components. Our analysis suggests that two types of M–M interactions should be considered in future structural studies: interactions which maintain the M dimer and may occur throughout the protein, and interactions between dimers which are probably mediated by the endodomains, which form a matrix-like layer underneath the membrane. In several ways, the function of coronavirus M appears be analogous to that of influenza A virus M1 protein, which shows pH-specific differences in membrane-bending

(Ruigrok et al., 1992). Crystallography studies have also revealed that M1 proteins have similar structures at acidic and neutral pH, but differ in the way protein monomers interact (Harris et al., 2001).

M of all coronaviruses appears to adopt an N-ecto/C-endo topology (Armstrong et al., 1984), but transmissible gastroenteritis coronavirus M also adopts an alternate N-endo/C-ecto topology (Risco et al., 1995). We initially considered that the difference between M_{LONG} and $M_{COMPACT}$ might be due to altered topology. The N-ecto/C-ecto topology proposed for TGEV M involves part of the endodomain forming a fourth transmembrane span, with part of the C-terminus exposed on the virion surface. Since the pre-transmembrane region of M is much smaller than the post-transmembrane region, an upside-down topology should be visually distinctive. However, the endodomains of M_{LONG} and $M_{COMPACT}$ were of similar size in class averages. Instead, we prefer an interpretation in which $M_{COMPACT}$ and M_{LONG} are conformationally distinct homodimers of N-ecto/C-endo topology, and the difference in appearance is due to a conformational change that either stretches (M_{LONG}) or collapses ($M_{COMPACT}$) the structure of the endodomain.

Prior to this study, the existence of reduction-sensitive complexes with a molecular weight consistent with approximately two, four and eight copies of M had been reported for HCoV-229E (Arpin and Talbot, 1990), but formation of a discrete M oligomer had not been demonstrated for any other coronavirus. The coronavirus M dimer would appear to be functionally equivalent to the heterodimeric complex of the triple-spanning membrane proteins GP5 and M which is essential for assembly of Equine arteritis virus (Snijder et al., 2003), a distantly related nidovirus. Further study of nidovirus ultrastructure is needed, but these observations coupled with the presence of one or more predicted three-transmembrane protein genes in every known coronavirus (M, but also SARS 3A and FCoV 3C), arterivirus (M and GP5), bafinivirus (GP4/M) and torovirus (M) genome suggests that dimeric complexes of triple-spanning membrane proteins may be a hallmark of nidovirus assembly.

While examining virions, we noticed that particles were most often either entirely spike-decorated or entirely spikeless. Further examination revealed that spikeless particles were significantly larger than spike-decorated particles, demonstrating that spikelessness resulted from a defect in assembly, not by accidental shearing or fusion activation. This led to a closer examination of SARS-CoV particles with patchy spike decoration. Spike patches were most often found at the ends of elongated particles, where M_{LONG} is common, suggesting that M_{LONG} mediates spike incorporation. Fig.10A shows a conceptual model of an elongated SARS-CoV particle with spikes decorating both ends, where M_{LONG} is plentiful. The association of small clusters of S with M_{LONG} was unexpected, but we were unable to determine whether the missing spikes were not incorporated, or were present in an elongated disordered conformation, as would be expected after fusion activation. Another possible explanation for this phenomenon is that incorporated spikes stabilize M_{LONG}.

There is some evidence to link the endodomain, which appears to undergo the most noticeable change between M_{LONG} and $M_{COMPACT}$, to incorporation of S protein. While the transmembrane region of M is important for M–S interactions, one residue of the M endodomain has been implicated in incorporation of S (de Haan et al., 1999). Mutation of a conserved tyrosine residue at position 211, near the N interaction site, does not affect VLP production but prevents S incorporation (de Haan et al., 1999). The C-terminus of the M endodomain shows the most profound structural difference between M_{LONG} and $M_{COMPACT}$. This suggests that tyrosine-211 may be important for M_{LONG} stability or for conversion between conformers. Further study is needed to determine the structural basis for coronavirus M, N and S protein interactions.
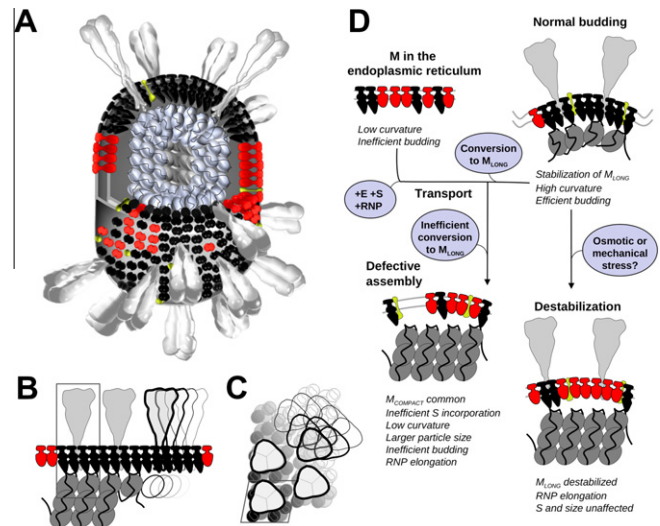

Fig. 10. Interpretation of coronavirus structure and assembly. (A) A schematic cutaway of an elongated SARS-CoV particle (size ≈ 85 nm, $d_{MAX}/d_{MIN} ≈ 1.4$) is shown to demonstrate how interactions between M_{LONG} (black), $M_{COMPACT}$ (white) and the ribonucleoprotein influence particle morphology. Spikes are shown in red and E protein oligomers in yellow. (B, C) Model for how M_{LONG} could be related to the spacing of spikes and RNP densities in edge view (B) and axial view (C). Hollow shapes mark the nearest potential attachment points for an additional spike or RNP density. (D) A flowchart presents a model for the role of M conformation in assembly. An additional path suggests and explanation for how particle morphology can be altered during purification.

By comparing M proteins on virus particles and VLPs, we identified N, S and genomic RNA as factors that increase the ratio of M_{LONG} to $M_{COMPACT}$. Properties attributed specifically to M_{LONG}, which include membrane rigidity, uniform curvature and spike incorporation, appear to be geared to assembly of infectious virus, and appear to be opposed by the properties of $M_{COMPACT}$. We would therefore hypothesize that factors or treatments which increase the relative abundance of M_{LONG} predict structural success, marked by increased virion fitness. Further work is needed to address the relationship between internal virion structure and infectivity.

4.1. Assessment of model quality

Protein spacing data presented here and previously (Neuman et al., 2006) suggests that eight dimeric M densities can accommodate a maximum of four N proteins and one trimeric spike protein, thus forming an $8M_2{:}4N{:}1S_3$ unit at the virion surface (see the boxed region in Figs.10B and C). We previously reported that the minimum spacing between spikes on highly decorated SARS-CoV particles was ∼14–15 nm, which is about 4–5 nm farther apart than would be expected based on the ∼10 nm width of each spike (Neuman et al., 2006). Fourier transformation revealed a ∼13–18 nm^{-1} frequency signal in tomographic projections of spike-decorated MHV, but not spikeless MHV, confirming that spike spacing for MHV-sp1 and SARS-CoV is similar (data not shown).

The diagrams in Figs.10B and C show a packing model in which adjacent spikes are incorporated at anchor points across the M_{LONG} network. Each M dimer could potentially interact with a spike, but the closest packing that could be achieved in this model would be ∼14–15 nm apart, based on the bulk of each spike and the nearest available anchor point. To test the quality of this model, we counted the number of spikes on three-dimensional reconstructions of MHV particles. These particles showed an average of 74 spikes per particle, which gives an approximate inter-spike spacing of 17 nm. Our model predicts ∼90 spikes per particle. Low spike incorporation in areas of $M_{COMPACT}$ may explain some of the difference between predicted and actual spike count.

The protein spacing model in Fig.10B and C shows an average spacing of 4–5 nm between M protein dimers. Using the M spacing data for each virus (Fig.6C), this would give ~1100 M_2 molecules per average SARS-CoV, MHV and FCoV particle. We are unable to directly count the number of M features per particle because of the resolution of the reconstructed tomograms. However, the ratio of M to N in purified coronavirus particles has been well studied, and provides an indirect way to test the validity of our proposed M_2 spacing. Estimated ratios of M to N protein in purified coronaviruses range from about 3M:1N (Cavanagh, 1983; Escors et al., 2001b) to 1M:1N (Hogue and Brian, 1986; Liu and Inglis, 1991), giving 730–2200 N molecules per virion. That works out to one N protein per 14–40 nucleotides of the genome. By comparison, the nucleoproteins of rabies virus and vesicular stomatitis virus are of similar molecular weight to coronavirus N proteins, and have been demonstrated to bind nine nucleotides per nucleoprotein (Albertini et al., 2006; Green et al., 2006). If, as suggested by Barcena et al. (2009), M dimers are spaced 6.5 nm apart, results of 60–200 nt/N molecule are obtained.

4.2. Model for coronavirus assembly

In the model of coronavirus assembly shown in Fig.10D, M is shown as a mixed population of M_{LONG} and $M_{COMPACT}$ in the endoplasmic reticulum membrane. M is then transported and interacts with other viral membrane proteins at the site of budding. The arrival of the ribonucleoprotein acts as a catalyst for the conversion of $M_{COMPACT}$ to M_{LONG}. The M_{LONG} densities bend the membrane to form a sphere around the ribonucleoprotein, with the size of the sphere inversely related to the relative abundance of M_{LONG}. Supplementary Fig.S5 relates virus particle size to membrane curvature per M dimer. We hypothesize that factors that interact with M such as N, S and genomic RNA could decrease particle size by limiting variation membrane curvature. After budding and release, environmental stress could convert some regions of M_{LONG} back to $M_{COMPACT}$, allowing the RNP to form longer helices and causing particle elongation.

The function of E in virogenesis remains poorly understood. It is interesting that the function and packaging of E and S are dependent on palmitin acylation (Boscarino et al., 2008; Lopez et al., 2008; Thorp et al., 2006), and further research will be needed to test whether M densities may contain one or more palmitin binding regions. Point mutations in E have been shown to result in the assembly of large, elongated, thermolabile MHV particles (Fischer et al., 1998). In light of the model proposed here, we would speculate that these characteristics can be attributed to an overabundance of packaged $M_{COMPACT}$, suggesting that E plays a role in promoting M_{LONG} formation or incorporation. This interpretation could be tested by cryo-EM and tomography of viruses carrying mutations in M and E.

5. Conclusions

In this study we described two functionally distinct forms of coronavirus M protein. Both types of M visible on viral particles were larger than expected for a single M protein, but consistent with the expected size of two M proteins. We demonstrated that M protein endodomains can self-assemble into oligo-dimeric complexes at 37 °C. We showed that formation of a convex, rigidified viral envelope is dependent on the presence of one form of M, which we have called M_{LONG}. Statistical evidence suggests that spike incorporation is linked to particle size, and that spikes cluster in regions where M_{LONG} is common. To explain these observations, we proposed a model in which locally-ordered networks of M_{LONG}, stabilized by S, N and possibly E proteins, control particle size and the efficiency of assembly.

Appendix A. Supplementary data

Supplementary data associated with this article can be found, in the online version, at doi:10.1016/j.jsb.2010.11.021.

References

Albertini, A.A., Wernimont, A.K., Muziol, T., Ravelli, R.B., Clapier, C.R., Schoehn, G., Weissenhorn, W., Ruigrok, R.W., 2006. Crystal structure of the rabies virus nucleoprotein-RNA complex. Science 313, 360–363.

Armstrong, J., Niemann, H., Smeekens, S., Rottier, P., Warren, G., 1984. Sequence and topology of a model intracellular membrane protein, E1 glycoprotein, from a coronavirus. Nature 308, 751–752.

Arpin, N., Talbot, P.J., 1990. Molecular characterization of the 229E strain of human coronavirus. Adv. Exp. Med. Biol. 276, 73–80.

Barcena, M., Oostergetel, G.T., Bartelink, W., Faas, F.G., Verkleij, A., Rottier, P.J., Koster, A.J., Bosch, B.J., 2009. Cryo-electron tomography of mouse hepatitis virus: insights into the structure of the coronavirion. Proc. Nat. Acad. Sci. USA 106, 582–587.

Beniac, D.R., Andonov, A., Grudeski, E., Booth, T.F., 2006. Architecture of the SARS coronavirus prefusion spike. Nat. Struct. Mol. Biol. 13, 751–752.

Boscarino, J.A., Logan, H.L., Lacny, J.J., Gallagher, T.M., 2008. Envelope protein palmitoylations are crucial for murine coronavirus assembly. J. Virol. 82, 2989–2999.

Carlson, L.A., Briggs, J.A., Glass, B., Riches, J.D., Simon, M.N., Johnson, M.C., Muller, B., Grunewald, K., Krausslich, H.G., 2008. Three-dimensional analysis of budding sites and released virus suggests a revised model for HIV-1 morphogenesis. Cell Host Microbe. 4, 592–599.

Cavanagh, D., 1983. Coronavirus IBV: further evidence that the surface projections are associated with two glycopolypeptides. J. Gen. Virol. 64, 1787–1791.

Chen, C.Y., Chang, C.K., Chang, Y.W., Sue, S.C., Bai, H.I., Riang, L., Hsiao, C.D., Huang, T.H., 2007. Structure of the SARS coronavirus nucleocapsid protein RNA-binding dimerization domain suggests a mechanism for helical packaging of viral RNA. J. Mol. Biol. 368, 1075–1086.

Davies, H.A., Macnaughton, M.R., 1979. Comparison of the morphology of three coronaviruses. Arch. Virol. 59, 25–33.

de Haan, C.A., Vennema, H., Rottier, P.J., 2000. Assembly of the coronavirus envelope: homotypic interactions between the M proteins. J. Virol. 74, 4967–4978.

de Haan, C.A., Smeets, M., Vernooij, F., Vennema, H., Rottier, P.J., 1999. Mapping of the coronavirus membrane protein domains involved in interaction with the spike protein. J. Virol. 73, 7441–7452.

Escors, D., Ortego, J., Laude, H., Enjuanes, L., 2001a. The membrane M protein carboxy terminus binds to transmissible gastroenteritis coronavirus core and contributes to core stability. J. Virol. 75, 1312–1324.

Escors, D., Camafeita, E., Ortego, J., Laude, H., Enjuanes, L., 2001b. Organization of two transmissible gastroenteritis coronavirus membrane protein topologies within the virion and core. J. Virol. 75, 12228–12240.

Fan, H., Ooi, A., Tan, Y.W., Wang, S., Fang, S., Liu, D.X., Lescar, J., 2005. The nucleocapsid protein of coronavirus infectious bronchitis virus: crystal structure of its N-terminal domain and multimerization properties. Structure 13, 1859–1868.

Fischer, F., Stegen, C.F., Masters, P.S., Samsonoff, W.A., 1998. Analysis of constructed E gene mutants of mouse hepatitis virus confirms a pivotal role for E protein in coronavirus assembly. J. Virol. 72, 7885–7894.

Frank, J., Radermacher, M., Penczek, P., Zhu, J., Li, Y., Ladjadj, M., Leith, A., 1996. SPIDER and WEB: processing and visualization of images in 3D electron microscopy and related fields. J. Struct. Biol. 116, 190–199.

Gallagher, T.M., Escarmis, C., Buchmeier, M.J., 1991. Alteration of the pH dependence of coronavirus-induced cell fusion: effect of mutations in the spike glycoprotein. J. Virol. 65, 1916–1928.

Green, T.J., Zhang, X., Wertz, G.W., Luo, M., 2006. Structure of the vesicular stomatitis virus nucleoprotein-RNA complex. Science 313, 357–360.

Harpaz, Y., Gerstein, M., Chothia, C., 1994. Volume changes on protein folding. Structure 2, 641–649.

Harris, A., Forouhar, F., Qiu, S., Sha, B., Luo, M., 2001. The crystal structure of the influenza matrix protein M1 at neutral pH: M1–M1 protein interfaces can rotate in the oligomeric structures of M1. Virology 289, 34–44.

Harris, A., Cardone, G., Winkler, D.C., Heymann, J.B., Brecher, M., White, J.M., Steven, A.C., 2006. Influenza virus pleiomorphy characterized by cryoelectron tomography. Proc. Natl. Acad. Sci. USA 103, 19123–19127.

Hogue, B.G., Brian, D.A., 1986. Structural proteins of human respiratory coronavirus OC43. Virus Res. 5, 131–144.

Hogue, B.G., Machamer, C.E., 2007. Coronavirus structural proteins and virus assembly. In: Perlman, S. et al. (Eds.), Nidoviruses. ASM Press, p, pp. 179–200.

Huang, Q., Yu, L., Petros, A.M., Gunasekera, A., Liu, Z., Xu, N., Hajduk, P., Mack, J., Fesik, S.W., Olejniczak, E.T., 2004. Structure of the N-terminal RNA-binding domain of the SARS CoV nucleocapsid protein. Biochemistry 43, 6059–6063.

Jayaram, H., Fan, H., Bowman, B.R., Ooi, A., Jayaram, J., Collisson, E.W., Lescar, J., Prasad, B.V., 2006. X-ray structures of the N- and C-terminal domains of a coronavirus nucleocapsid protein: implications for nucleocapsid formation. J. Virol. 80, 6612–6620.

Klumperman, J., Locker, J.K., Meijer, A., Horzinek, M.C., Geuze, H.J., Rottier, P.J., 1994. Coronavirus M proteins accumulate in the Golgi complex beyond the site of virion budding. J. Virol. 68, 6523–6534.

Knoops, K., Kikkert, M., Worm, S.H., Zevenhoven-Dobbe, J.C., van der Meer, Y., Koster, A.J., Mommaas, A.M., Snijder, E.J., 2008. SARS-coronavirus replication is supported by a reticulovesicular network of modified endoplasmic reticulum. PLoS Biol. 6, e226.

Kremer, J.R., Mastronarde, D.N., McIntosh, J.R., 1996. Computer visualization of three-dimensional image data using IMOD. J. Struct. Biol. 116, 71–76.

Kunding, A.H., Mortensen, M.W., Christensen, S.M., Stamou, D., 2008. A fluorescence-based technique to construct size distributions from single-object measurements: application to the extrusion of lipid vesicles. Biophys. J. 95, 1176–1188.

Kuo, L., Masters, P.S., 2002. Genetic evidence for a structural interaction between the carboxy termini of the membrane and nucleocapsid proteins of mouse hepatitis virus. J. Virol. 76, 4987–4999.

Lee, Y.N., Chen, L.K., Ma, H.C., Yang, H.H., Li, H.P., Lo, S.Y., 2005. Thermal aggregation of SARS-CoV membrane protein. J. Virol. Methods 129, 152–161.

Li, F., Li, W., Farzan, M., Harrison, S.C., 2005. Structure of SARS coronavirus spike receptor-binding domain complexed with receptor. Science 309, 1864–1868.

Liu, D.X., Inglis, S.C., 1991. Association of the infectious bronchitis virus 3c protein with the virion envelope. Virology 185, 911–917.

Lokugamage, K.G., Yoshikawa-Iwata, N., Ito, N., Watts, D.M., Wyde, P.R., Wang, N., Newman, P., Kent Tseng, C.T., Peters, C.J., Makino, S., 2008. Chimeric coronavirus-like particles carrying severe acute respiratory syndrome coronavirus (SCoV) S protein protect mice against challenge with SCoV. Vaccine 26, 797–808.

Lopez, L.A., Riffle, A.J., Pike, S.L., Gardner, D., Hogue, B.G., 2008. Importance of conserved cysteine residues in the coronavirus envelope protein. J. Virol. 82, 3000–3010.

Ludtke, S.J., Baldwin, P.R., Chiu, W., 1999. EMAN: semiautomated software for high-resolution single-particle reconstructions. J. Struct. Biol. 128, 82–97.

Machamer, C.E., Rose, J.K., 1987. A specific transmembrane domain of a coronavirus E1 glycoprotein is required for its retention in the Golgi region. J. Cell Biol. 105, 1205–1214.

Nagle, J.F., Tristram-Nagle, S., 2000. Structure of lipid bilayers. Biochim. Biophys. Acta 1469, 159–195.

Nal, B., Chan, C., Kien, F., Siu, L., Tse, J., Chu, K., Kam, J., Staropoli, I., Crescenzo-Chaigne, B., Escriou, N., van der Werf, S., Yuen, K.Y., Altmeyer, R., 2005. Differential maturation and subcellular localization of severe acute respiratory syndrome coronavirus surface proteins S, M and E. J. Gen. Virol. 86, 1423–1434.

Narayanan, K., Maeda, A., Maeda, J., Makino, S., 2000. Characterization of the coronavirus M protein and nucleocapsid interaction in infected cells. J. Virol. 74, 8127–8134.

Narayanan, K., Chen, C.J., Maeda, J., Makino, S., 2003. Nucleocapsid-independent specific viral RNA packaging via viral envelope protein and viral RNA signal. J. Virol. 77, 2922–2927.

Neuman, B.W., Adair, B.D., Yeager, M., Buchmeier, M.J., 2008a. Purification and electron cryomicroscopy of coronaviruses. In: Cavanagh, D. (Ed.), SARS and Other Coronaviruses: Laboratory Protocols. Humana Press, New York, pp. 129–138.

Neuman, B.W., Adair, B.D., Burns, J.W., Milligan, R.A., Buchmeier, M.J., Yeager, M., 2005. Complementarity in the supramolecular design of arenaviruses and retroviruses revealed by electron cryomicroscopy and image analysis. J. Virol. 79, 3822–3830.

Neuman, B.W., Adair, B.D., Yoshioka, C., Quispe, J.D., Orca, G., Kuhn, P., Milligan, R.A., Yeager, M., Buchmeier, M.J., 2006. Supramolecular architecture of severe acute respiratory syndrome coronavirus revealed by electron cryomicroscopy. J. Virol. 80, 7918–7928.

Neuman, B.W., Joseph, J.S., Saikatendu, K.S., Serrano, P., Chatterjee, A., Johnson, M.A., Liao, L., Klaus, J.P., Yates 3rd, J.R., Wüthrich, K., Stevens, R.C., Buchmeier, M.J., Kuhn, P., 2008b. Proteomics analysis unravels the functional repertoire of coronavirus nonstructural protein 3. J. Virol. 82, 5279–5294.

Nguyen, V.P., Hogue, B.G., 1997. Protein interactions during coronavirus assembly. J. Virol. 71, 9278–9284.

Opstelten, D.J., Raamsman, M.J., Wolfs, K., Horzinek, M.C., Rottier, P.J., 1995. Envelope glycoprotein interactions in coronavirus assembly. J. Cell Biol. 131, 339–349.

Pervushin, K., Tan, E., Parthasarathy, K., Lin, X., Jiang, F.L., Yu, D., Vararattanavech, A., Soong, T.W., Liu, D.X., Torres, J., 2009. Structure and inhibition of the SARS coronavirus envelope protein ion channel. PLoS Pathog. 5, e1000511.

Ramjeesingh, M., Huan, L.J., Garami, E., Bear, C.E., 1999. Novel method for evaluation of the oligomeric structure of membrane proteins. Biochem. J. 342, 119–123.

Risco, C., Anton, I.M., Enjuanes, L., Carrascosa, J.L., 1996. The transmissible gastroenteritis coronavirus contains a spherical core shell consisting of M and N proteins. J. Virol. 70, 4773–4777.

Risco, C., Anton, I.M., Sune, C., Pedregosa, A.M., Martin-Alonso, J.M., Parra, F., Carrascosa, J.L., Enjuanes, L., 1995. Membrane protein molecules of transmissible gastroenteritis coronavirus also expose the carboxy-terminal region on the external surface of the virion. J. Virol. 69, 5269–5277.

Rottier, P.J., Rose, J.K., 1987. Coronavirus E1 glycoprotein expressed from cloned cDNA localizes in the Golgi region. J. Virol. 61, 2042–2045.

Ruigrok, R.W., Hewat, E.A., Wade, R.H., 1992. Low pH deforms the influenza virus envelope. J. Gen. Virol. 73, 995–998.

Saikatendu, K.S., Joseph, J.S., Subramanian, V., Neuman, B.W., Buchmeier, M.J., Stevens, R.C., Kuhn, P., 2007. Ribonucleocapsid formation of severe acute respiratory syndrome coronavirus through molecular action of the N-terminal domain of N protein. J. Virol. 81, 3913–3921.

Sawicki, S.G., 1987. Characterization of a small plaque mutant of the A59 strain of mouse hepatitis virus defective in cell fusion. Adv. Exp. Med. Biol. 218, 169–174.

Schutze, H., Ulferts, R., Schelle, B., Bayer, S., Granzow, H., Hoffmann, B., Mettenleiter, T.C., Ziebuhr, J., 2006. Characterization of white bream virus reveals a novel genetic cluster of nidoviruses. J. Virol. 80, 11598–11609.

Snijder, E.J., Dobbe, J.C., Spaan, W.J., 2003. Heterodimerization of the two major envelope proteins is essential for arterivirus infectivity. J. Virol. 77, 97–104.

Stewart, A., Grigorieff, N., 2004. Noise bias in the refinement of structures derived from single particles. Ultramicroscopy 102, 67–84.

Sticht, J., Humbert, M., Findlow, S., Bodem, J., Muller, B., Dietrich, U., Werner, J., Krausslich, H.G., 2005. A peptide inhibitor of HIV-1 assembly in vitro. Nat. Struct. Mol. Biol. 12, 671–677.

Sturman, L.S., Holmes, K.V., Behnke, J., 1980. Isolation of coronavirus envelope glycoproteins and interaction with the viral nucleocapsid. J. Virol. 33, 449–462.

Suloway, C., Pulokas, J., Fellmann, D., Cheng, A., Guerra, F., Quispe, J., Stagg, S., Potter, C.S., Carragher, B., 2005. Automated molecular microscopy: the new Leginon system. J. Struct. Biol. 151, 41–60.

Tang, C., Loeliger, E., Kinde, I., Kyere, S., Mayo, K., Barklis, E., Sun, Y., Huang, M., Summers, M.F., 2003. Antiviral inhibition of the HIV-1 capsid protein. J. Mol. Biol. 327, 1013–1020.

Thorp, E.B., Boscarino, J.A., Logan, H.L., Goletz, J.T., Gallagher, T.M., 2006. Palmitoylations on murine coronavirus spike proteins are essential for virion assembly and infectivity. J. Virol. 80, 1280–1289.

Vennema, H., Godeke, G.J., Rossen, J.W., Voorhout, W.F., Horzinek, M.C., Opstelten, D.J., Rottier, P.J., 1996. Nucleocapsid-independent assembly of coronavirus-like particles by co-expression of viral envelope protein genes. EMBO J. 15, 2020–2028.

Zeng, Q., Langereis, M.A., van Vliet, A.L., Huizinga, E.G., de Groot, R.J., 2008. Structure of coronavirus hemagglutinin-esterase offers insight into corona and influenza virus evolution. Proc. Natl. Acad. Sci. USA 105, 9065–9069.

Zhong-can, O.Y., Helfrich, W., 1987. Instability and deformation of a spherical vesicle by pressure. Phys. Rev. Lett. 59, 2486–2488.